Polarization-Driven Asymmetric Electronic Response of Monolayer Graphene to Polymer Zwitterions Probed from Both Sides

Nicholas Hight-Huf, $^{\dagger \S}$ Yehiel Nagar, $^{\bot \S}$ Adi Levi, $^{\bot}$ James Nicolas Pagaduan, ‡ Avdhoot Datar, $^{\parallel}$ Reika Katsumata, ‡ Todd Emrick, ‡ Ashwin Ramasubramaniam, $^{\parallel}$ Doron Naveh, $^{\bot}$ and Michael D. Barnes $^{\dagger = *}$

†Department of Chemistry, **Department of Physics, **Polymer Science and Engineering Department, and ||Department of Mechanical and Industrial Engineering, University of Massachusetts, Amherst, MA 01003, USA

⊥Faculty of Engineering and Institute for Nanotechnology and Advanced Materials, Bar-Ilan University, Ramat-Gan 52900, Israel

*Corresponding Author, to whom all inquiries should be addressed §These authors contributed equally to this manuscript

Abstract

We investigated the nature of graphene surface doping by zwitterionic polymers and the implications of weak in-plane and strong through-plane screening using a novel sample geometry that allows direct access to either the graphene or the polymer side of a graphene/polymer interface. Using both Kelvin probe and electrostatic force microscopies, we observed a significant upshift in the Fermi level in graphene of ≈ 260 meV that was dominated by a change in polarizability rather than pure charge transfer with the organic overlayer. This physical picture is supported by density functional theory (DFT) calculations which describe a redistribution of charge in graphene in response to the dipoles of the adsorbed zwitterionic moieties, analogous to a local DC Stark effect. Strong metallic-like screening of the adsorbed dipoles was observed by employing an inverted geometry, an effect identified by DFT to arise from a strongly asymmetric redistribution of charge confined to the side of graphene proximal to the zwitterion dipoles. Transport measurements

confirm n-type doping with no significant impact on carrier mobility, thus demonstrating a route to desirable electronic properties in devices that combine graphene with lithographically patterned polymers.

Keywords: Hybrid 2D materials, KPFM, EFM, charge transfer, polarizability, screening, graphene, zwitterion, lithography, FET

2D materials, such as graphene and transition metal dichalcogenides (TMDCs), represent an emerging platform for next-generation electronics^{1–3} and sensor technologies,^{4–7} as well as for examination of new physics involving spintronics and valleytronics.^{8–10} Despite the growing body of research pointing to the merits of 2D materials, several challenges must be overcome for such materials to achieve widespread use. First, new strategies must be discovered that both provide effective electrical modification of the 2D structure and ensure its protection from undesired impurities such as gases¹¹ and water.¹² Second, the significant differences in properties of 2D materials relative to bulk structures, such as electrical transport¹³ and screening,¹⁴ challenge us to develop new models and characterization techniques to understand the connection between surface interactions and electronic properties.

An ideal effective strategy for 2D materials doping would provide a substantial change in carrier density/Fermi level, not hinder electrical transport, and remain stable over time. One prominent strategy is to coat the 2D materials with an organic overlayer. The key to controlling electronic properties, such as Fermi energy, band alignment, and carrier density, lies in the interactions between the organic layer (typically functioning as a charge dopant) and the 2D material. Such hybrid materials can be divided into a chemical functionalization^{15–20} (covalent surface

modification) group and a non-covalent group.^{21–26} Additional approaches to the electronic modification of 2D materials include substitutional doping^{27–32} and ferroelectric gating.^{33–35} We view non-covalent surface modification as an attractive doping strategy without disrupting the pristine 2D layer, while also providing an opportunity for lithographic patterning and improved processability.^{24,26} Although ferroelectric gating is attractive for producing addressable circuit elements, our non-covalent hybrid materials approach is driven by applications where the additional circuitry needed to produce the forming and coercive fields represents undesired complexity along with concerns for the stability of the electronic properties of interest. While we previously reported non-covalent charge doping in graphene using sulfobetaine zwitterions,^{24,26} here we find phosphorylcholine (PC) -substituted polymers, of the type typically employed in non-fouling coatings,³⁶ to have a remarkable impact on graphene that, as we describe, is chemically and electronically distinct from typical dopant adsorbates.

Obtaining mechanistic details is crucial to characterizing 2D materials and interfaces, which stems from the fact that the most common surface techniques lack sufficient depth specificity. Additionally imperative is to understand how screening within 2D materials evolves in response to the surrounding environment, and in turn the impact of the surrounding environment on electrical measurements made on the 2D material (i.e., due to dielectric screening). Unlike 3D electronic materials, which have electronic properties dictated by bulk structure, 2D materials properties depend strongly on the nature of the surrounding material with which it comes into contact. For graphene, charge screening through the thickness of a monolayer is strong due to the semi-metallic nature of the charge carriers in graphene, resulting in a very short screening length (effectively on the order of the thickness of monolayer graphene). In-plane screening, however, contains significant contributions from the out-of-plane electric fields, which are weakly affected

by the surrounding dielectric resulting in a much longer screening length, but are more susceptible to variations in dielectric constant of this environment.^{37–39} This combination leads to screening through the plane of monolayer graphene that is stronger by orders of magnitude than screening in-plane, with in-plane screening depending closely on the makeup of the support and surface of graphene devices.^{37–39}

Like other 2D materials, electrostatic screening in graphene results from non-local, many-body Coulombic interactions. Unlike the complete Faradaic screening of *ideal* 2D metals, the finite screening of graphene stems from intralayer Coulombic interactions that couple charge density and polarizability. ^{14,40} In prior work by others, the connection between screening and polarization in graphene has been studied using substrates such as SiO₂, ^{38,41,42} metal oxides as gate dielectrics ^{38,42} and electrolytic top gates. ⁴² Screening is also tied to a material's conductivity which, together with polarizability, is a key performance element for graphene-based bio- and chemical sensors. ⁴³ Recent progress in the preparation of polymer-containing graphene devices includes doping by ultrathin polymer layers ^{24,26} and fabrication of free-standing polymer-supported graphene membranes. ⁴⁴ A combination of such strategies, as described here, allowed for more direct probing of the graphene–polymer interface for the first time without perturbation associated with the thickness of the organic layer. Previous observations have shown that overlayer thickness has a complex impact on surface electronic measurements, ²⁶ and thus minimizing this influence is of great interest.

In this work, we employed scanning probe methods to examine polymer-coated graphene samples *from both sides*, which generated evidence of a polarization-driven doping mechanism and an enhanced understanding of screening effects in graphene in response to the surrounding environment. This insight was gained by employing Electric Force Microscopy (EFM), which

differentiates between changes in surface charge and polarizability due to interactions between the graphene and polymer. Our results are in accord with DFT calculations, which predicted no charge transfer between graphene and the PC moiety of the selected polymer zwitterions. Observations of screening within graphene were obtained by comparing potential measurements made on a second inverted sample geometry, giving access to the "flip side", i.e., opposite to the zwitterion dipoles. The weak charge screening by the surrounding dielectric media was observed at the depletion region, formed at adjacent regions with and without polymer contact, using Kelvin probe force microscopy (KPFM). As described, we employed a variety of experimental and theoretical methods to gain insight into surface dipole interactions as well as key properties that differ from bulk semiconductor junctions such as 2D screening effects. 14,37

The "normal" and "inverted" orientations of a hybrid graphene/organic field-effect transistor (FET) are illustrated in Figure 1 a,b. The platform features lithographically patterned doped regions which provides an in situ reference for scanning probe methods, and the opportunity to examine the behavior at the boundaries of those regions. As the organic overlayer, we selected poly(methacryloyloxyethyl phosphorylcholine) (PMPC) as a copolymer with methyl methacrylate and crosslinkable benzophenone methacrylate comonomers (Figure 1c). Unlike previous hybrid 2D systems which show clear evidence of charge-doping, ^{21–25,45–49} we find that the dominant effect in this PMPC copolymer/graphene system is a change in polarization due to dipole interactions, i.e., a shift in the Fermi level in response to the PC dipoles (Figure 1d).

Electric force and electric force-gradient scanning probe methods were used to assess the electronic properties of the polymer-coated monolayer graphene, which was supported on Si/SiO₂ substrates. Kelvin probe force microscopy (KPFM) is an electric force method^{21–23,25,48,49} which tracks changes in the Fermi level of a material or interface by measuring a contact potential

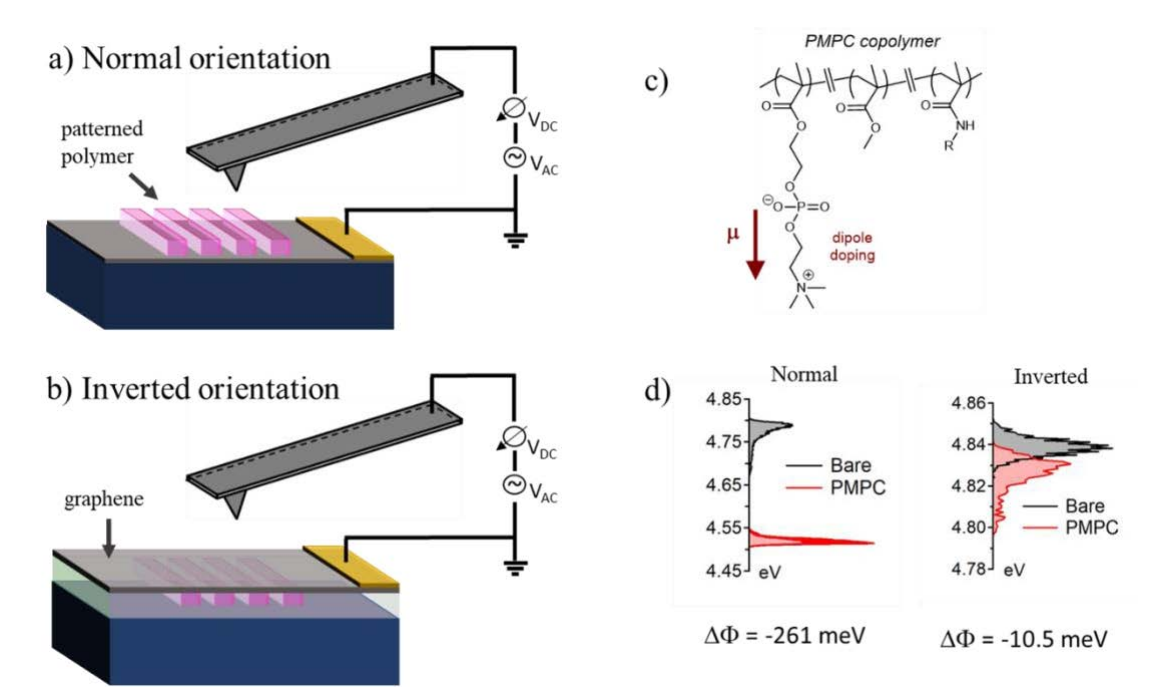


Figure 1. Schematic of samples in two measurement configurations: (a) lithographically patterned polymer (depicted in pink) on graphene in a 'normal' orientation; (b) polymer underneath and graphene facing the probe in an 'inverted' orientation'. (c) Chemical structure of the polymer zwitterion, where R represents benzophenone moieties responsible for photocrosslinking. (d) Work function distributions of bare and polymer-coated regions of the normal and inverted orientations. High-quality electrical measurements with a well-defined ground were enabled by evaporating gold contacts directly onto the graphene.

difference (CPD).⁵⁰ EFM is sensitive to electric force-gradients,^{51–53} enabling measurement of spatially dependent information about the polarizability and effective surface charge.⁵⁴ Virtually all examples of hybrid 2D materials involving non-covalently associated organic overlayers assume a model in which the organic material acts as an n- or p-type charge dopant.^{21–25,45–49,55} Although doping of 2D materials involves altering the free carrier density through charge exchange with a dopant, being able to locally tune carrier density with high spatial precision represents a major potential advantage for the sharp transitions in carrier density necessary to produce p-n homojunctions. Polarization in response to polymer dipoles at the graphene surface is predicted to play a role analogous to an electrolytic gate,⁴² including a superior capacitance due to the close proximity of these dipoles to the graphene surface, compared to a typical oxide gate. Such an approach could be combined with electrical gating to achieve independent control of both the

global carrier density needed for achieving acceptable device performance, and the local carrier density variation required to create 2D homojunctions and minimize Schottky barriers at metallic contacts. EFM and KPFM results for this polymer-graphene system together demonstrated that changes in the Fermi energy derive primarily from image-charge interactions with pendant zwitterionic moieties on the polymer, with only a small component due to charge doping. Correlations between experimental results and computer simulations confirm this effect and suggest further tuning of the electronic interactions could be achieved via control over dipole orientation, thus obviating the need for charge transfer.

The PMPC copolymer was synthesized by reversible addition-fragmentation chain transfer (RAFT) copolymerization of MPC with methyl methacrylate (MMA) and a photo-crosslinkable benzophenone methacrylamide (BPMA) (details are given in section S1of the supporting information). Use of MMA as a comonomer enhances polymer film formation relative to PMPC itself, while the cross-linking capabilities of the benzophenone group facilitate production of negative tone resists. The copolymer had a 42:55:3 molar ratio of [MPC]:[MMA]:[BPMA], as determined by ¹H NMR spectroscopy (Figure S1). The number-average molecular weight of the copolymer used in our experiments was 19.8 kDa and the polydispersity index (Đ) was 1.11 (Figure S3). The detailed production of doped samples is given in the supporting information (sections S3, S4, of S.I.). Briefly, the PMPC copolymer was applied by spin-coating from 2,2,2trifluoroethanol onto monolayer CVD graphene supported by a Si/SiO2 substrate. The PMPC copolymer was then patterned by e-beam lithography. A 'normal' orientation sample (Figure 1a) was prepared by evaporating gold contacts directly onto the graphene layer. An 'inverted' orientation (Figure 1b) sample was prepared by casting a polycarbonate membrane over the patterned sample, then etching the underlying oxide layer with HF; the free-standing membrane

was retrieved and inverted onto a fresh Si/SiO₂ substrate (Figure S4), and finally gold contacts were applied to the graphene evaporative deposition.

Electronic characterization was performed using a combination of KPFM and EFM. In KPFM measurements, a PtIr-coated Si probe (AppNano ANSCM-PT, $f_0 \sim 71$ kHz) operating in tapping mode, acquired surface topography in a first pass; the CPD due to capacitive forces between the sample and the tip were measured in a second pass performed at a lift height of 30 nm, chosen to minimize short range forces between the polymer dipoles and the tip. Here, CPD is defined as the work function difference between the probe and the sample (e $V_{CPD} = \Phi_{probe} - \Phi_{sample}$, where e is the fundamental charge, and Φ is work function). This relationship can also be viewed as tracking the Fermi level of the sample, where an increase in CPD (i.e., a more positive value), yields an increase in the Fermi level (i.e., closer to the vacuum level). CPD measurements were converted to work function values, by measuring a highly oriented pyrolytic graphite standard to calibrate the probe's work function. In the EFM measurements, the second pass was used to record the phase shift of the cantilever and was repeated several times at various tip biases. At each point of the area scanned, the phase shift vs. tip bias was fit to a quadratic model (Figure S7), where the linear and quadratic terms encode information on surface charge and polarizability, respectively.⁵⁴

Figure 2a,b shows the surface height and calibrated work function for polymer-coated graphene in the 'normal orientation' (polymer overlayer up). KPFM line traces across the polymer boundary reveal a clear increase in the Fermi level (Figure 1c), corresponding to a work function reduction of 261 meV relative to bare graphene (by the difference in work function distributions given in Figure 1d, i.e., n-type doping). We note that there is a contribution to the measured surface potential due to an interaction between the tip and the dipoles. The strength of these long range

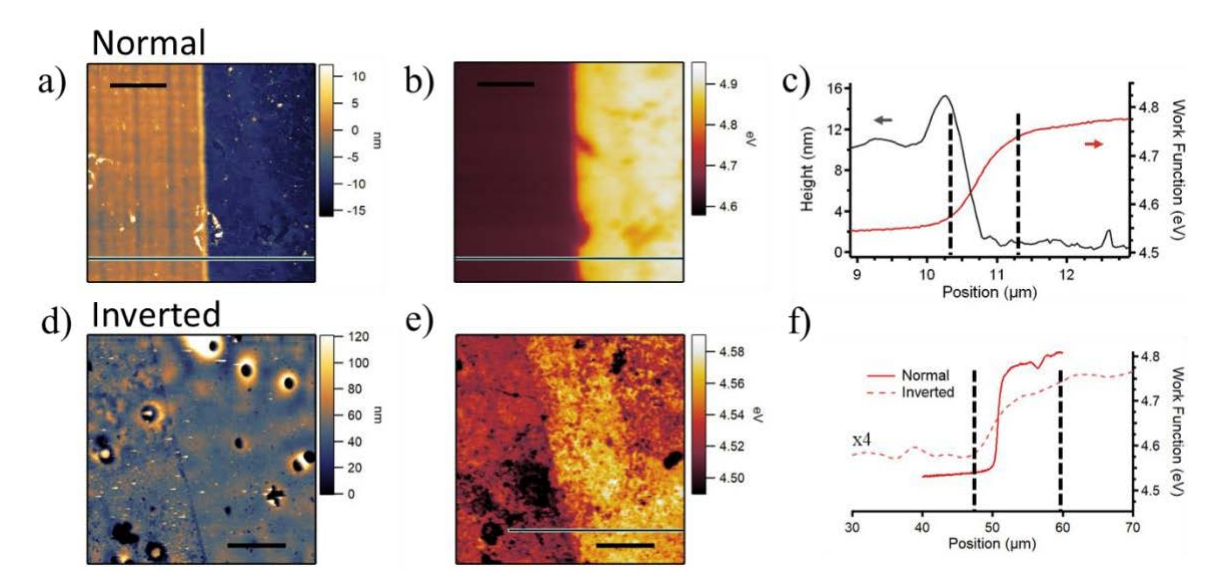


Figure 2. Maps of (a) normal orientation topography and (b) calibrated work function by KPFM, scale bars indicate 5 μ m. (c) Overlaid topography (black, scale left) and work function profiles (red, scale right), taken from the lines indicated in the KPFM height and work function maps shown in a,b. Maps of (d) inverted orientation topography and (e) calibrated work function by KPFM, scale bars indicate 25 μ m In both sample orientations the low work function region at the left of the figure (b,e) is due to the polymer, and the transition to lower surface potentials is at the boundary of this region. (f) Work function line scans from b,e showing a more gradual transition in the inverted sample due weaker screening of out-of-plane electric fields according to the different dielectric environment. In f, the inverted trace has been shifted and expanded by a factor of 4 in the y coordinate (the x-coordinate has not been modified), for ease of comparison.

(Coulombic) forces is expected to be small due to the nearly flat dipole orientation that DFT predicts (as detailed below), in which contributions from the negative and positive end of the dipole nearly cancel. The strength of these long-range forces has been estimated by performing KPFM on a polymer film prepared on a different conducting substrate, ITO, but otherwise in an analogous manner, which yielded a value of ~ 10 meV (Figure S6). Figure 2d,e shows the surface height and work function for the inverted orientation (graphene side up). In this configuration, Coulombic interactions between the dipoles and tip are minimized, and dielectric screening of the graphene/polymer interface by the polymer has been removed, (i.e., where the electric field between two charged surfaces is attenuated due to the polarization of a dielectric medium). The measured CPD variation due to polymer coverage is quite small compared to the normal orientation sample, ~10 meV (Figure S5c), which speaks to the strength of the semi-metallic

screening in graphene compared to dielectric screening and interactions between the dipoles and the tip. The strong screening within graphene masks the interaction between the polymer zwitterions and the underside of graphene, when measured on the top side. In addition, substrate effects have been shown to decrease the apparent magnitude of doping molecules at the surface,²⁵ which we believe plays a smaller role relative to the screening in graphene.

The KPFM measurements also presented a unique opportunity to investigate the potential profile at a 2D p-n junction (determination of carrier profiles shown later). The depletion width across the polymer-covered to bare portions of graphene was on the order of 1.1 µm (Figure 2c, red curve). Despite the sharp spatial profile of the polymer topography (Figure 2c, black curve), the potential variation due to the polarization of graphene by the zwitterionic moieties was less localized. The inverted sample has a depletion width approximately 12 µm which is an order of magnitude larger (Figure 2f). These widths reflect two important aspects of 2D p-n junctions that differ from that of bulk semiconductors. First, the contact between the two regions forms a line rather than a plane, which affects charge exchange and the distance dependence of the potential about this interface.³⁷ Second, there is a significant out-of-plane electric field generated by the space charge region formed on either side of this line, which is only modestly screened by the surrounding dielectric environment when compared to traditional bulk semiconductors. ^{37,56–58} The increased width of the inverted orientation, can be attributed to the decrease in the dielectric constant of the underlying substrate from 3.9 (SiO₂ normal orientation) to 2.9 (polycarbonate). Due to the relative scarcity of depletion width measurements across lateral 2D p-n junctions, results such as those shown here are valuable for refining theories of electrostatics and for developing production techniques for devices based on 2D architectures. Future work is planned to investigate the impact on the depletion width and the associated screening due to the

environment using different polymer layers. Such investigations might yield routes to increase the depletion width to improve photosensor collection, or decrease it to manage resistive losses at metallic contacts.

In addition to KPFM mapping of the electrochemical potential associated with graphenepolymer interactions including charge transfer, we employed EFM measurements which provide the second moment of electric force to map variations in polarizability and surface charge. Our EFM measurements revealed a statistically significant contrast (5.4 σ and 6.7 σ for the normal and inverted samples, respectively) in the polarizability of graphene due contact with the polymer, which was clearly observable in both the normal and inverted sample orientations (Figure 3 a,b,e). The surface charge term reveals that in the normal sample, bare graphene is p-type with doping attributed to interactions with the Si/SiO₂ substrate.^{39,59-61} The inverted sample, on the other hand, experiences a small amount of charge donation from the polycarbonate substrate, resulting in ntype graphene prior to treatment with the polymer zwitterions. In each configuration, graphene experiences a modest increase in electron density due to the presence of the polymer as indicated by surface charge (Figure 3 c,d,f). From the surface charge measurements, a shift in the Fermi level can be calculated based on the relationship between carrier density and Fermi level according to $E_F = \hbar v_F \sqrt{n_D \pi}$, where E_F is the Fermi level, v_F is the Fermi velocity, and n_D is the carrier density. Using this approach, we determined a work function shift of 24 meV in the normal orientation sample due to a change in surface charge. This is in stark contrast to the KPFM shift of 261 meV for the same orientation sample, which implies the presence of an additional dominant mechanism to account for the total shift in the electrochemical potential. The difference between the change in surface charge of the two orientations due to the polymer is a product of screening within graphene and mirrors the results of KPFM which contains a coulombic contribution. The

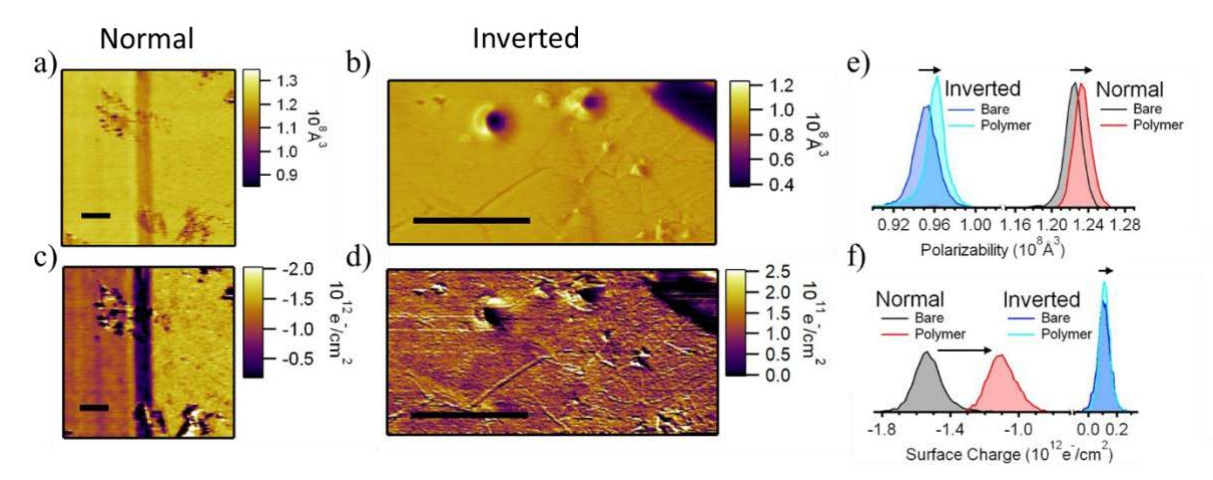


Figure 3. Maps of the polarizability obtained through EFM of the (a) normal orientation and (b) inverted samples, in both cases the PMPC region is on the left and bare region is on the right. Maps of the surface charge of (c) normal and (d) inverted samples. Scale bars in a-d indicate 2.5 μ m. Distributions of (e) polarizability, and (f) surface charge at the graphene surface of both normal and inverted geometry samples, derived from images a-d. Statistically significant increases in polarizability are observed for both samples, 5.4 σ and 6.7 σ for the normal and inverted samples, respectively. Arrows in e,f indicate the direction and magnitude of changes due to the polymer.

adsorbed surface charge on the underside of the inverted geometry sample is effectively hidden by the charge carriers in graphene. The combination of small changes in surface charge and an increase in polarizability leads us to conclude that image-charge formation is responsible for the Fermi level shift observed by KPFM. This shift due to polarization also fits the conclusions of DFT modeling (described in the next section).

We modeled the interaction of the dipolar moiety with graphene, considering four different dipolar orientations (Figure S8) that may be present in the samples produced. Since no attempts were made experimentally to manipulate the dipole orientation in the samples prepared, the dipoles should assume the lowest energy configuration in the absence of significant kinetic barriers. The calculated most stable orientation is shown in Figure 4a, where the pendant group containing the negatively charged phosphate is nearest the graphene sheet, while the positively charged ammonium group is located further from the sheet due to a steric effect of the surrounding methyl groups. Figure 4 highlights the polarization in graphene due to a zwitterionic moiety in the lowest energy orientation (with respect to surface normal) obtained from DFT calculations. In our

computational model, we considered the interaction of PC groups with a freestanding 6×6 supercell of a graphene monolayer (Figure 4a). We neglected the polymer backbone in our computational model for the sake of tractability and, instead, terminated the dipolar moiety with a methyl group. Our prior work has shown this approximation to yield results that agree qualitatively with experimental measurements.^{24,26} Analogous to the familiar problem of a static dipole near a metal surface, 62,63 the adsorption of the pendent zwitterion on graphene results in a net dipole moment with a perpendicular component $\mu_{\perp} = 0.52$ D. This total dipole moment is slightly smaller than the corresponding dipole moment of the isolated moiety frozen at the same adsorption configuration ($\mu_{\perp} = 0.65$ D) and this difference is attributed to charge redistribution at the zwitterion/graphene interface. Figure 4b displays the resulting charge redistribution upon physisorption of the dipolar moiety on graphene, from which we note complementary regions of charge accumulation (yellow) and depletion (cyan), correlated with the positive and negative ends of the adsorbed dipole, respectively. This charge redistribution is localized to a few unit cells proximal to the adsorbed moiety and, importantly, is not accompanied by any net charge transfer, an effect which EFM measurements confirm is minor compared to polarization effects. The surface dipole resulting from the adsorbed zwitterion induces a small upshift of the Fermi level of graphene (i.e., reduced work function) as seen from the upshift of the charge-neutrality point in graphene (Figure 4c) as well as the differences in the planar-averaged Hartree potentials on the two sides of the graphene sheet, i.e., with and without the adsorbed PC group (Figure 4d). We note that the work function on the side without the dipole (Figure 4d) is identical to pristine graphene, in agreement with the near complete screening of the dipole observed in EFM measurements of inverted samples. The calculated 100 meV work function decrease is in qualitative agreement with experiment, although the magnitude is smaller than the measured value (261 meV by KPFM, 227

meV by transport measurements); quantitative discrepancies might be expected from a lack of disorder in dipole orientation within the DFT model (see section S7), neglect of the polymer film and underlying substrate, and accuracy of the DFT exchange-correlation functionals, among others.

To investigate the implications of the observed graphene polarization due to the presence of PMPC copolymer, graphene FET devices with three different polymer coverages (fully covered, partially covered, and no coverage) were fabricated and measured (Figure 5a-c). All three devices

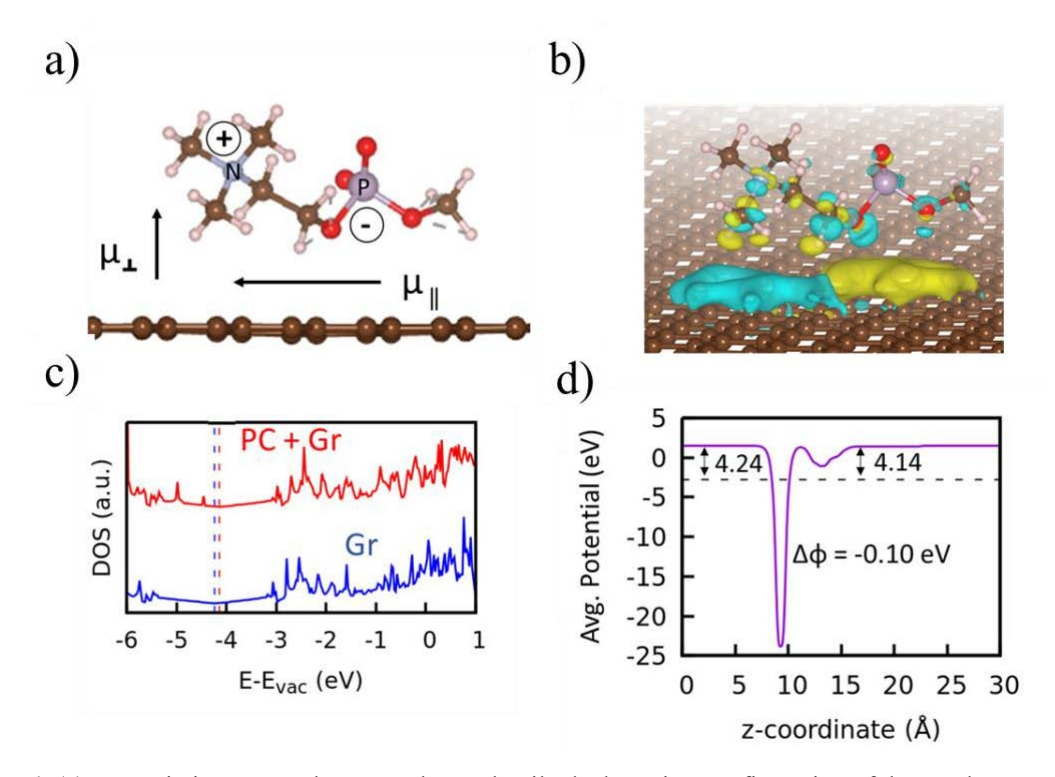


Figure 4. (a) PC moietiy on monolayer graphene: the tilted adsorption configuration of the pendent group leads to both transverse (μ|) and normal (μ_⊥) components of dipole moment. White, brown, blue, violet, and red spheres indicate H, C, N, P, and O atoms, respectively. (b) Charge-difference plot for PC adsorbed on a graphene sheet; yellow/cyan isosurfaces ($\pm 5 \times 10^{-4}$ e⁻/Å³) indicate charge accumulation/depletion. (c) Total density of states (red line) for PC + graphene sheet (PC + Gr) and (blue line) for a bare graphene sheet (Gr). All energies are reported relative to the vacuum level (0 eV); dotted lines indicate the Fermi level for each system (d) Planar-averaged Hartree potential along z-direction (normal to graphene sheet) for a graphene sheet with adsorbed PC; dotted line indicates the position of the Fermi level from which we infer the indicated work functions (Φ) with respect to the vacuum potential.

were measured by the four-point probe method to determine the influence of the PMPC copolymer on graphene's carrier density and mobility. The charge-neutrality point of the fully covered device was shifted by ~ 38 V compared to the uncovered device, corresponding to an increase in electron density of $\Delta n \approx 2.73 \times 10^{12}$ e⁻/cm² induced by PMPC copolymer. The location of the charge-neutrality point changed from a positive gate voltage in the PMPC-free device to a negative gate voltage in the fully covered device, indicating a change in the majority carriers from holes (p-type) to electrons (n-type), respectively, in agreement with EFM measurements. The carrier mobility as a function of gate voltage of the three devices is shown in Figure 5d, peaking at the neutrality point of each device and relaxing to values of 1100-1400 cm²/Vs. Therefore, we infer that the effects of PMPC copolymer on carrier mobility are limited, while the impact on the local carrier density is significant, corresponding to a work function reduction of >200 meV. These values agree well with KPFM results (261 meV). The significant doping due to polymer coverage, combined with sufficient localization of carrier density resulted in a p-n homojunction with good mobility. Further tuning of electronic properties through the modification of dipole orientation, via steric

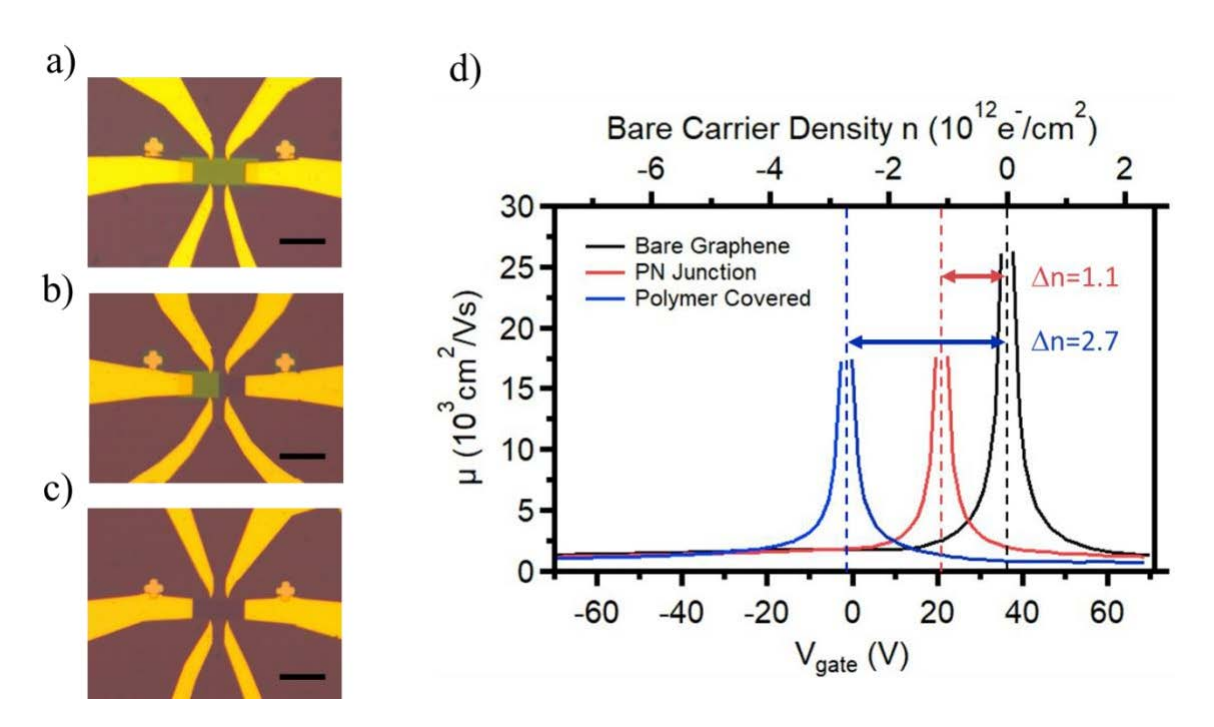


Figure 5. Optical micrographs of the (a) fully covered, (b) half covered, and (c) bare graphene devices. The scale bars in a-c indicate $25 \, \mu m$. (d) Mobility as function of gate bias of the three devices (lower scale) and the charge carrier density of the bare graphene (upper scale).

effects to manipulation of side chains,²⁶ or electric poling, will provide additional opportunities to explore the impacts of variation in work function and polarization on device performance.

The results presented here show the efficacy of a 2D materials doping strategy as evaluated by a combination of scanning probe methods, transport measurements, and modeling techniques. In these new types of hybrid organic/inorganic 2D material, the electronics are dictated primarily by an image-charge interaction between the pendant dipolar moieties of the zwitterionic polymer and graphene; in contrast with observations of other systems^{22,23,25} in which the electronic properties are attributed to p- or n-type charge doping. We have shown that zwitterionic polymer overlayers interact non-covalently with graphene and shift its Fermi energy towards the conduction band (an effect conventionally associated with n-type doping), independently of minor influences from charge injection. EFM results unambiguously demonstrate a lack of surface charges required for the observed shift in Fermi level by a purely charge-doping mechanism. This is further supported by DFT modeling, which shows that the Fermi level shift derives from an induced dipole at graphene's surface that depends on the overlayer dipole orientation. By employing both inverted and normal configurations, we were able to observe directly by KPFM and EFM the strong metallic-like screening of the pendant dipole, which decreased the apparent charge and surface potential in inverted measurements. In contrast, in plane screening was relatively weaker, where KPFM shows >90% of the variation in electric potential occurs within ~ 500 nm laterally of the bare-polymer interface in the normal sample and ~10x this distance for the inverted sample, which we attribute to 2D screening effects which depend on the dielectric environment. In both cases, extended tails persist for several µm, a unique look at a 2D p-n homojunction formed using a zwitterionic polymer. As a new class of hybrid 2D materials, understanding how electronic properties depend on the orientation of the surface dipoles suggests exciting new possibilities for

further tuning by control of dipole orientation (i.e., by electric field poling). The combination of

lithographic patterning and localized electronic modification makes the use of zwitterion-based

resists attractive for device fabrication with feature sizes on the order of tens of nanometers.

Overall, our findings are significant for advancing chemical and biological sensing applications of

graphene, where the electrostatic screening is the central parameter for device performance⁴³.

Supporting Information

Synthetic methods and characterization of the monomers and polymers; fabrication of devices;

details of **KPFM** and EFM; and further details of **DFT** calculations.

Corresponding Author

*E-mail: mdbarnes@chem.umass.edu

Author Contributions

All of the authors contributed to the preparation of this manuscript. N.H.H. and M.D.B.

performed KPFM and EFM measurements. J.N.P., R.K., and T.E. synthesized and characterized

the monomers and polymers, prepared samples. A.D. and A.R. conducted the computational

analysis. D.N. and Y.N. performed the device fabrication and measurements. All authors have

given approval to the final version of the manuscript. N.H.H. and Y.N. contributed equally.

Notes

The authors declare no competing financial interests.

Acknowledgments

We gratefully acknowledge the National Science Foundation (NSF-BSF 1808011) and the US-

Israel Binational Science Foundation (2017655) for support. J.N.P. thanks PPG Industries, Inc.

17

for the 2018–2019 PPG Foundation Fellowship. R.K. expresses gratitude for startup funding from UMass Amherst. A.D. and A.R. acknowledge computational support from the Extreme Science and Engineering Discovery Environment (XSEDE), which is supported by National Science Foundation grant number ACI-1548562.

References

- (1) Areshkin, D. A.; White, C. T. Building Blocks for Integrated Graphene Circuits. *Nano Lett.* **2007**, 7 (11), 3253–3259.
- (2) Schwierz, F. Graphene Transistors. *Nat. Nanotechnol.* **2010**, *5* (7), 487–496.
- (3) Wang, H.; Yu, L.; Lee, Y.-H.; Shi, Y.; Hsu, A.; Chin, M. L.; Li, L.-J.; Dubey, M.; Kong, J.; Palacios, T. Integrated Circuits Based on Bilayer MoS2 Transistors. *Nano Lett.* **2012**, *12* (9), 4674–4680.
- (4) Levi, A.; Kirshner, M.; Sinai, O.; Peretz, E.; Meshulam, O.; Ghosh, A.; Gotlib, N.; Stern, C.; Yuan, S.; Xia, F.; Naveh, D. Graphene Schottky Varactor Diodes for High-Performance Photodetection. ACS Photonics 2019, 6 (8), 1910–1915.
- (5) Xia, F.; Mueller, T.; Golizadeh-Mojarad, R.; Freitag, M.; Lin, Y.; Tsang, J.; Perebeinos, V.; Avouris, P. Photocurrent Imaging and Efficient Photon Detection in a Graphene Transistor. *Nano Lett.* **2009**, *9* (3), 1039–1044.
- (6) Cheng, R.; Jiang, S.; Chen, Y.; Liu, Y.; Weiss, N.; Cheng, H.-C.; Wu, H.; Huang, Y.; Duan, X. Few-Layer Molybdenum Disulfide Transistors and Circuits for High-Speed Flexible Electronics. *Nat. Commun.* 2014, 5 (1), 5143.
- (7) Hang, Y.; Li, Q.; Luo, W.; He, Y.; Zhang, X.; Peng, G. Photo-Electrical Properties of

- Trilayer MoSe2 Nanoflakes. *Nano* **2016**, *11* (07), 1650082.
- (8) Mak, K. F.; He, K.; Shan, J.; Heinz, T. F. Control of Valley Polarization in Monolayer MoS2 by Optical Helicity. *Nat. Nanotechnol.* 2012, 7, 494.
- (9) Zeng, H.; Dai, J.; Yao, W.; Xiao, D.; Cui, X. Valley Polarization in MoS2 Monolayers by Optical Pumping. *Nat. Nanotechnol.* **2012**, *7* (8), 490–493.
- (10) Cao, T.; Wang, G.; Han, W.; Ye, H.; Zhu, C.; Shi, J.; Niu, Q.; Tan, P.; Wang, E.; Liu, B.; Feng, J. Valley-Selective Circular Dichroism of Monolayer Molybdenum Disulphide. *Nat. Commun.* **2012**, *3* (1), 887.
- (11) Panchal, V.; Giusca, C. E.; Lartsev, A.; Martin, N. A.; Cassidy, N.; Myers-Ward, R. L.; Gaskill, D. K.; Kazakova, O. Atmospheric Doping Effects in Epitaxial Graphene: Correlation of Local and Global Electrical Studies. *2D Mater.* **2016**, *3* (1), 15006.
- (12) Shim, J.; Lui, C. H.; Ko, T. Y.; Yu, Y.-J.; Kim, P.; Heinz, T. F.; Ryu, S. Water-Gated Charge Doping of Graphene Induced by Mica Substrates. *Nano Lett.* **2012**, *12* (2), 648–654.
- (13) Sangwan, V. K.; Hersam, M. C. Electronic Transport in Two-Dimensional Materials. *Annu. Rev. Phys. Chem.* **2018**, *69* (1), 299–325.
- (14) Ambrosetti, A.; Silvestrelli, P. L. Faraday-like Screening by Two-Dimensional Nanomaterials: A Scale-Dependent Tunable Effect. *J. Phys. Chem. Lett.* **2019**, *10* (9), 2044–2050.
- (15) Arellano, L. M.; Yue, S.; Atienzar, P.; Gómez-Escalonilla, M. J.; Ortega-Higueruelo, F. J.; Fierro, J. L. G.; García, H.; Langa, F. Modulating Charge Carrier Density and Mobility in Doped Graphene by Covalent Functionalization. *Chem. Commun.* **2019**, *55* (67), 9999–

10002.

- (16) Sarkar, S.; Bekyarova, E.; Haddon, R. C. Covalent Chemistry in Graphene Electronics. *Mater. Today* **2012**, *15* (6), 276–285.
- (17) Zhang, H.; Bekyarova, E.; Huang, J.-W.; Zhao, Z.; Bao, W.; Wang, F.; Haddon, R. C.; Lau,
 C. N. Aryl Functionalization as a Route to Band Gap Engineering in Single Layer Graphene
 Devices. *Nano Lett.* 2011, *11* (10), 4047–4051.
- (18) Azcatl, A.; Qin, X.; Prakash, A.; Zhang, C.; Cheng, L.; Wang, Q.; Lu, N.; Kim, M. J.; Kim, J.; Cho, K.; Addou, R.; Hinkle, C. L.; Appenzeller, J.; Wallace, R. M. Covalent Nitrogen Doping and Compressive Strain in MoS2 by Remote N2 Plasma Exposure. *Nano Lett.* 2016, 16 (9), 5437–5443.
- (19) Canton-Vitoria, R.; Sayed-Ahmad-Baraza, Y.; Pelaez-Fernandez, M.; Arenal, R.; Bittencourt, C.; Ewels, C. P.; Tagmatarchis, N. Functionalization of MoS2 with 1,2-Dithiolanes: Toward Donor-Acceptor Nanohybrids for Energy Conversion. *npj 2D Mater*. *Appl.* 2017, *I* (1), 13.
- (20) Wang, Y.; Qi, L.; Shen, L.; Wu, Y. Surface Defect Passivation of MoS2 by Sulfur, Selenium, and Tellurium. *J. Appl. Phys.* **2016**, *119* (15), 154301.
- (21) Wang, X.; Xu, J.-B.; Xie, W.; Du, J. Quantitative Analysis of Graphene Doping by Organic Molecular Charge Transfer. *J. Phys. Chem. C* **2011**, *115* (15), 7596–7602.
- (22) Selhorst, R. C.; Puodziukynaite, E.; Dewey, J. A.; Wang, P.; Barnes, M. D.; Ramasubramaniam, A.; Emrick, T. Tetrathiafulvalene-Containing Polymers for Simultaneous Non-Covalent Modification and Electronic Modulation of MoS(2)

- Nanomaterials. Chem. Sci. 2016, 7 (7), 4698–4705.
- (23) Selhorst, R.; Wang, P.; Barnes, M.; Emrick, T. Bithiazolidinylidene Polymers: Synthesis and Electronic Interactions with Transition Metal Dichalcogenides. *Chem. Sci.* **2018**, *9* (22), 5047–5051.
- (24) Alon, H.; Stern, C.; Kirshner, M.; Sinai, O.; Wasserman, M.; Selhorst, R.; Gasper, R.; Ramasubramaniam, A.; Emrick, T.; Naveh, D. Lithographically Patterned Functional Polymer–Graphene Hybrids for Nanoscale Electronics. ACS Nano 2018, 12 (2), 1928–1933.
- (25) Wang, P.; Selhorst, R.; Emrick, T.; Ramasubramaniam, A.; Barnes, M. D. Bidirectional Electronic Tuning of Single-Layer MoS2 with Conjugated Organochalcogens. *J. Phys. Chem. C* **2019**, *123* (2), 1506–1511.
- (26) Pagaduan, J. N.; Hight-Huf, N.; Datar, A.; Nagar, Y.; Barnes, M.; Naveh, D.; Ramasubramaniam, A.; Katsumata, R.; Emrick, T. Electronic Tuning of Monolayer Graphene with Polymeric "Zwitterists." *ACS Nano* **2021**, *15* (2), 2762–2770.
- (27) Lv, R.; Li, Q.; Botello-Méndez, A. R.; Hayashi, T.; Wang, B.; Berkdemir, A.; Hao, Q.; Elías, A. L.; Cruz-Silva, R.; Gutiérrez, H. R.; Kim, Y. A.; Muramatsu, H.; Zhu, J.; Endo, M.; Terrones, H.; Charlier, J.-C.; Pan, M.; Terrones, M. Nitrogen-Doped Graphene: Beyond Single Substitution and Enhanced Molecular Sensing. *Sci. Rep.* 2012, 2 (1), 586.
- (28) Cervantes-Sodi, F.; Csányi, G.; Piscanec, S.; Ferrari, A. C. Edge-Functionalized and Substitutionally Doped Graphene Nanoribbons: Electronic and Spin Properties. *Phys. Rev. B* **2008**, 77 (16), 165427.
- (29) Jeong, H. M.; Lee, J. W.; Shin, W. H.; Choi, Y. J.; Shin, H. J.; Kang, J. K.; Choi, J. W.

- Nitrogen-Doped Graphene for High-Performance Ultracapacitors and the Importance of Nitrogen-Doped Sites at Basal Planes. *Nano Lett.* **2011**, *11* (6), 2472–2477.
- Gao, J.; Kim, Y. D.; Liang, L.; Idrobo, J. C.; Chow, P.; Tan, J.; Li, B.; Li, L.; Sumpter, B.
 G.; Lu, T.-M.; Meunier, V.; Hone, J.; Koratkar, N. Transition-Metal Substitution Doping in
 Synthetic Atomically Thin Semiconductors. *Adv. Mater.* 2016, 28 (44), 9735–9743.
- (31) Mahjouri-Samani, M.; Lin, M.-W.; Wang, K.; Lupini, A. R.; Lee, J.; Basile, L.; Boulesbaa, A.; Rouleau, C. M.; Puretzky, A. A.; Ivanov, I. N.; Xiao, K.; Yoon, M.; Geohegan, D. B. Patterned Arrays of Lateral Heterojunctions within Monolayer Two-Dimensional Semiconductors. *Nat. Commun.* **2015**, *6*, 7749.
- Zhang, K.; Bersch, B. M.; Joshi, J.; Addou, R.; Cormier, C. R.; Zhang, C.; Xu, K.; Briggs,
 N. C.; Wang, K.; Subramanian, S.; Cho, K.; Fullerton-Shirey, S.; Wallace, R. M.; Vora, P.
 M.; Robinson, J. A. Tuning the Electronic and Photonic Properties of Monolayer MoS2 via
 In Situ Rhenium Substitutional Doping. Adv. Funct. Mater. 2018, 28 (16), 1706950.
- (33) Zheng, Y.; Ni, G.-X.; Toh, C.-T.; Tan, C.-Y.; Yao, K.; Özyilmaz, B. Graphene Field-Effect Transistors with Ferroelectric Gating. *Phys. Rev. Lett.* **2010**, *105* (16), 166602.
- (34) Bae, S.-H.; Kahya, O.; Sharma, B. K.; Kwon, J.; Cho, H. J.; Özyilmaz, B.; Ahn, J.-H. Graphene-P(VDF-TrFE) Multilayer Film for Flexible Applications. *ACS Nano* **2013**, *7* (4), 3130–3138.
- (35) Ni, G.-X.; Zheng, Y.; Bae, S.; Tan, C. Y.; Kahya, O.; Wu, J.; Hong, B. H.; Yao, K.; Özyilmaz, B. Graphene–Ferroelectric Hybrid Structure for Flexible Transparent Electrodes. *ACS Nano* **2012**, *6* (5), 3935–3942.

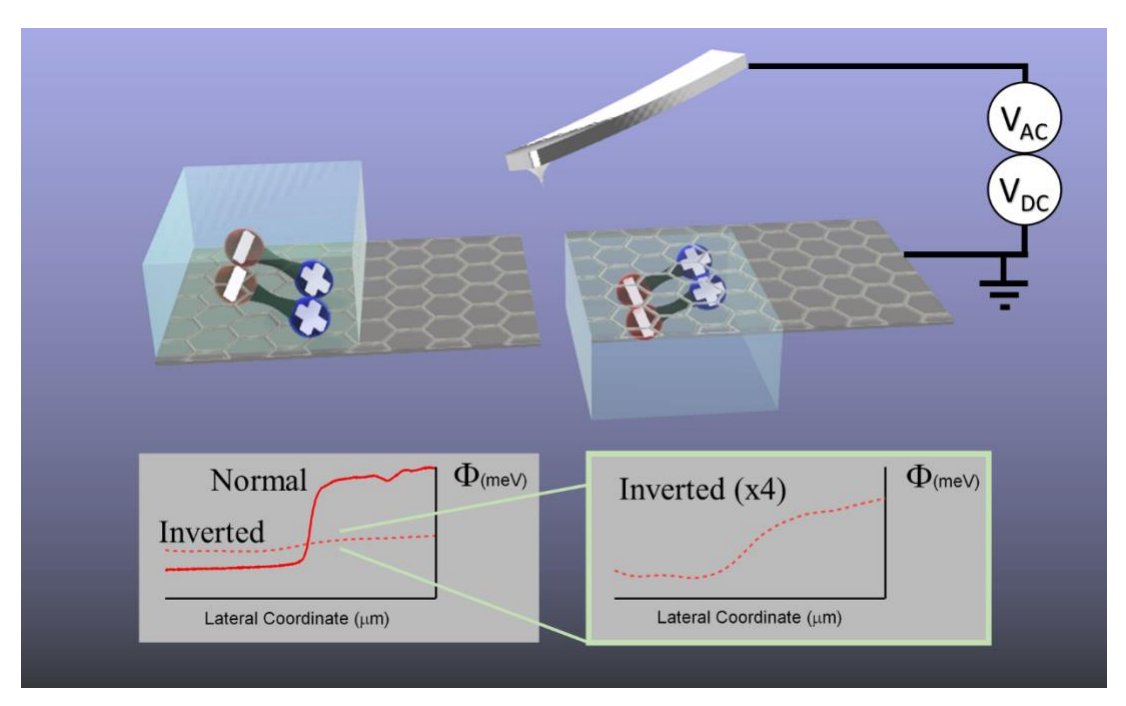
- (36) Kratz, K.; Xie, W.; Lee, A.; Freeman, B. D.; Emrick, T. Phosphorylcholine-Substituted ROMP Polyolefin Coatings Provide Fouling Resistance to Membrane Materials. *Macromol. Mater. Eng.* 2011, 296 (12), 1142–1148.
- (37) Yu, H.; Kutana, A.; Yakobson, B. I. Carrier Delocalization in Two-Dimensional Coplanar p–n Junctions of Graphene and Metal Dichalcogenides. *Nano Lett.* **2016**, *16* (8), 5032–5036.
- (38) Ghaznavi, M.; Mišković, Z. L.; Goodman, F. O. Nonlinear Screening of External Charge by Doped Graphene. *Phys. Rev. B* **2010**, *81* (8), 85416.
- (39) Wang, R.; Wang, S.; Zhang, D.; Li, Z.; Fang, Y.; Qiu, X. Control of Carrier Type and Density in Exfoliated Graphene by Interface Engineering. *ACS Nano* **2011**, *5* (1), 408–412.
- (40) Guinea, F. Charge Distribution and Screening in Layered Graphene Systems. *Phys. Rev. B* **2007**, 75 (23), 235433.
- (41) de Andres, P. L.; Echenique, P. M.; Niesner, D.; Fauster, T.; Rivacoba, A. One-Dimensional Potential for Image-Potential States on Graphene. *New J. Phys.* **2014**, *16* (2), 23012.
- (42) Sharma, P.; Mišković, Z. L. Ionic Screening of Charged Impurities in Electrolytically Gated Graphene: A Partially Linearized Poisson-Boltzmann Model. *J. Chem. Phys.* **2015**, *143* (13), 134118.
- (43) Fu, W.; Jiang, L.; van Geest, E. P.; Lima, L. M. C.; Schneider, G. F. Sensing at the Surface of Graphene Field-Effect Transistors. *Adv. Mater.* **2017**, *29* (6), 1603610.
- (44) Khan, A. U.; Zeltzer, G.; Speyer, G.; Croft, Z. L.; Guo, Y.; Nagar, Y.; Artel, V.; Levi, A.; Stern, C.; Naveh, D.; Liu, G. Mutually Reinforced Polymer–Graphene Bilayer Membranes for Energy-Efficient Acoustic Transduction. *Adv. Mater.* **2021**, *33* (2), 2004053.

- (45) Miao, X.; Tongay, S.; Petterson, M. K.; Berke, K.; Rinzler, A. G.; Appleton, B. R.; Hebard,
 A. F. High Efficiency Graphene Solar Cells by Chemical Doping. *Nano Lett.* 2012, *12* (6),
 2745–2750.
- (46) Zhang, S.; Le, S. T.; Richter, C. A.; Hacker, C. A. Improved Contacts to P-Type MoS2 Transistors by Charge-Transfer Doping and Contact Engineering. *Appl. Phys. Lett.* 2019, 115 (7), 73106.
- (47) Wang, X.; Xie, W.; Chen, J.; Xu, J.-B. Homo- and Hetero- p-n Junctions Formed on Graphene Steps. ACS Appl. Mater. Interfaces 2014, 6 (1), 3-8.
- (48) Zhou, X.; He, S.; Brown, K. A.; Mendez-Arroyo, J.; Boey, F.; Mirkin, C. A. Locally Altering the Electronic Properties of Graphene by Nanoscopically Doping It with Rhodamine 6G. *Nano Lett.* **2013**, *13* (4), 1616–1621.
- (49) Yoo, H.; Hong, S.; On, S.; Ahn, H.; Lee, H.-K.; Hong, Y. K.; Kim, S.; Kim, J.-J. Chemical Doping Effects in Multilayer MoS2 and Its Application in Complementary Inverter. *ACS Appl. Mater. Interfaces* **2018**, *10* (27), 23270–23276.
- (50) Melitz, W.; Shen, J.; Kummel, A. C.; Lee, S. Kelvin Probe Force Microscopy and Its Application. *Surf. Sci. Rep.* **2011**, *66* (1), 1–27.
- (51) Howell, S. L.; Jariwala, D.; Wu, C.-C.; Chen, K.-S.; Sangwan, V. K.; Kang, J.; Marks, T. J.; Hersam, M. C.; Lauhon, L. J. Investigation of Band-Offsets at Monolayer–Multilayer MoS2 Junctions by Scanning Photocurrent Microscopy. *Nano Lett.* 2015, *15* (4), 2278–2284.
- (52) Karolline A. S. Araujo, Luiz A. Cury, Matheus J. S. Matos, Thales F. D. Fernandes, L. G.

- C. and B. R. A. N. Electro-Optical Interfacial Effects on a Graphene/π-Conjugated Organic Semiconductor Hybrid System. *Beilstein J. Nanotechnol.* **2018**, *9*, 963–974.
- (53) Hofmann, M.; Hsieh, Y.-P.; Chang, K.-W.; Tsai, H.-G.; Chen, T.-T. Dopant Morphology as the Factor Limiting Graphene Conductivity. *Sci. Rep.* **2015**, *5* (1), 17393.
- (54) Kim, J.; Jasper, W. J.; Hinestroza, J. P. Charge Characterization of an Electrically Charged Fiber via Electrostatic Force Microscopy. *J. Eng. Fiber. Fabr.* **2006**, *1* (2), 155892500600100200.
- (55) Kiriya, D.; Tosun, M.; Zhao, P.; Kang, J. S.; Javey, A. Air-Stable Surface Charge Transfer Doping of MoS2 by Benzyl Viologen. *J. Am. Chem. Soc.* **2014**, *136* (22), 7853–7856.
- (56) Maheswaran, K. R. K.; Karmalkar, S. Effect of the Ambient Field on the I–V Characteristics of Nanowire Resistors and Junctions—A Simulation Study. *Phys. E Low-dimensional Syst.*Nanostructures 2011, 44 (3), 700–707.
- (57) Nipane, A.; Jayanti, S.; Borah, A.; Teherani, J. T. Electrostatics of Lateral P-n Junctions in Atomically Thin Materials. *J. Appl. Phys.* **2017**, *122* (19), 194501.
- (58) Gurugubelli, V. K.; Karmalkar, S. Analytical Theory of the Space-Charge Region of Lateral p-n Junctions in Nanofilms. *J. Appl. Phys.* **2015**, *118* (3), 34503.
- (59) Casiraghi, C.; Pisana, S.; Novoselov, K. S.; Geim, A. K.; Ferrari, A. C. Raman Fingerprint of Charged Impurities in Graphene. *Appl. Phys. Lett.* **2007**, *91* (23), 233108.
- (60) Goniszewski, S.; Adabi, M.; Shaforost, O.; Hanham, S. M.; Hao, L.; Klein, N. Correlation of P-Doping in CVD Graphene with Substrate Surface Charges. *Sci. Rep.* **2016**, *6* (1), 22858.

- (61) Berciaud, S.; Ryu, S.; Brus, L. E.; Heinz, T. F. Probing the Intrinsic Properties of Exfoliated Graphene: Raman Spectroscopy of Free-Standing Monolayers. *Nano Lett.* **2009**, *9* (1), 346–352.
- (62) Holmström, S.; Holloway, S. The Interaction of a Dipole with a Metal Surface. Surf. Sci.1986, 173 (2), L647–L654.
- (63) Gabovich, A. M.; Li, M. S.; Szymczak, H.; Voitenko, A. I. Image Forces for a Point-like Dipole near a Plane Metal Surface: An Account of the Spatial Dispersion of Dielectric Permittivity. *Surf. Sci.* **2012**, *606* (3), 510–515.

For Table of Contents Only



SUPPORTING INFORMATION

Polarization-Driven Asymmetric Electronic Response of Monolayer Graphene to Polymer Zwitterions Probed from Both Sides

Nicholas Hight-Huf,†§ Yehiel Nagar, ¹§ Adi Levi, ¹ James Nicolas Pagaduan,‡ Avdhoot Datar, □ Reika Katsumata, ‡ Todd Emrick, ‡ Ashwin Ramasubramaniam, □ Doron Naveh, ¹ and Michael Barnes† **

†Department of Chemistry, Department of Physics, ‡Polymer Science and Engineering Department, and ||Department of Mechanical and Industrial Engineering, University of Massachusetts, Amherst, MA 01003, USA

⊥ Faculty of Engineering and Institute for Nanotechnology and Advanced Materials, Bar-Ilan University, Ramat-Gan 52900, Israel

1. Synthesis of Poly(2-Methacryloyloxyethyl phosphorylcholine-co-methyl methacrylate-co-benzophenone methacrylamide) or P(MPC-MMA-BPMA)

2-Methacryloyloxyethyl phosphorylcholine (MPC, 97%), methyl methacrylate (MMA, 99%), 4-cyano-4-(phenylcarbonothioylthio)pentanoic acid (CTA), and 2,2'-azobisisobutyronitrile (AIBN, 98%) were purchased from Sigma-Aldrich (St. Louis, MO, USA). Benzophenone methacrylamide (BPMA) was prepared as in previous report.\(^1\) 2,2,2-trifluoroethanol (TFE, 99.9%) was obtained from Oakwood Products, Inc (West Columbia, SC, USA). Before use, MPC was purified using diethyl ether, MMA was run through a plug of basic alumina to remove the inhibitor, and AIBN was recrystallized from methanol. Other materials were used as received. The PMPC copolymer was synthesized via RAFT polymerization with a molar feed ratio of MPC: MMA: BPMA = 50 (1.71 g): 47 (0.55 g): 3 (93 mg). The monomers were mixed in TFE (11.6 mL) in a 50-mL round bottom flask charged with a magnetic stir bar. CTA (10.9 mg) and AIBN initiator (0.6 mg) were then added, and the reaction mixture was purged with N2 for 30 minutes. The reaction was allowed to proceed at 80°C for 18 hours. The resulting copolymer was precipitated into diethyl ether, centrifuged, and dried under vacuum at room temperature for 24 hours. Dialysis in deionized water was performed for three days to remove unreacted monomers. The final product was afforded after freeze-drying (Yield: 72%, TFE GPC with PMMA standards: Mn = 19 kDa, \(\theta\) = 1.11).

Scheme S1. Preparation of P(MPC-MMA-BPMA) by RAFT polymerization.

¹H NMR (500 MHz) spectra of the polymer products were recorded on a Bruker AscendTM 500 spectrometer equipped with a Prodigy cryoprobe. Size-exclusion chromatography (SEC, using PMMA calibration standards) was conducted using an eluent mixture of TFE with 0.02 M sodium trifluoroacetate at 40 °C on an Agilent 1200 system equipped with the following: an isocratic pump operated at 1 mL/min, a degasser, an autosampler, one 50 mm × 8 mm PSS PFG guard column (Polymer Standards Service), and three 300 mm × 7.5 mm PSS PFG analytical linear M columns with 7 μm particle size (Polymer Standards Service), and an Agilent 1200 refractive index detector.

Table S1. Summary of characterization data for prepared P(MPC-MMA-BPMA) random copolymer.

Polymer	Feed Ratio	Actual Ratio ^a	Yield	M _n ^b	PDIb
	[MPC]:[MMA]:[BPMA]		(%)	(kDa)	PDI
P(MPC-MMA-BPMA)	50:47:3	42:55:3	72	19.8	1.11

a) Determined by ¹H NMR spectroscopy; b) Estimated by SEC relative to PMMA standards, eluting in TFE

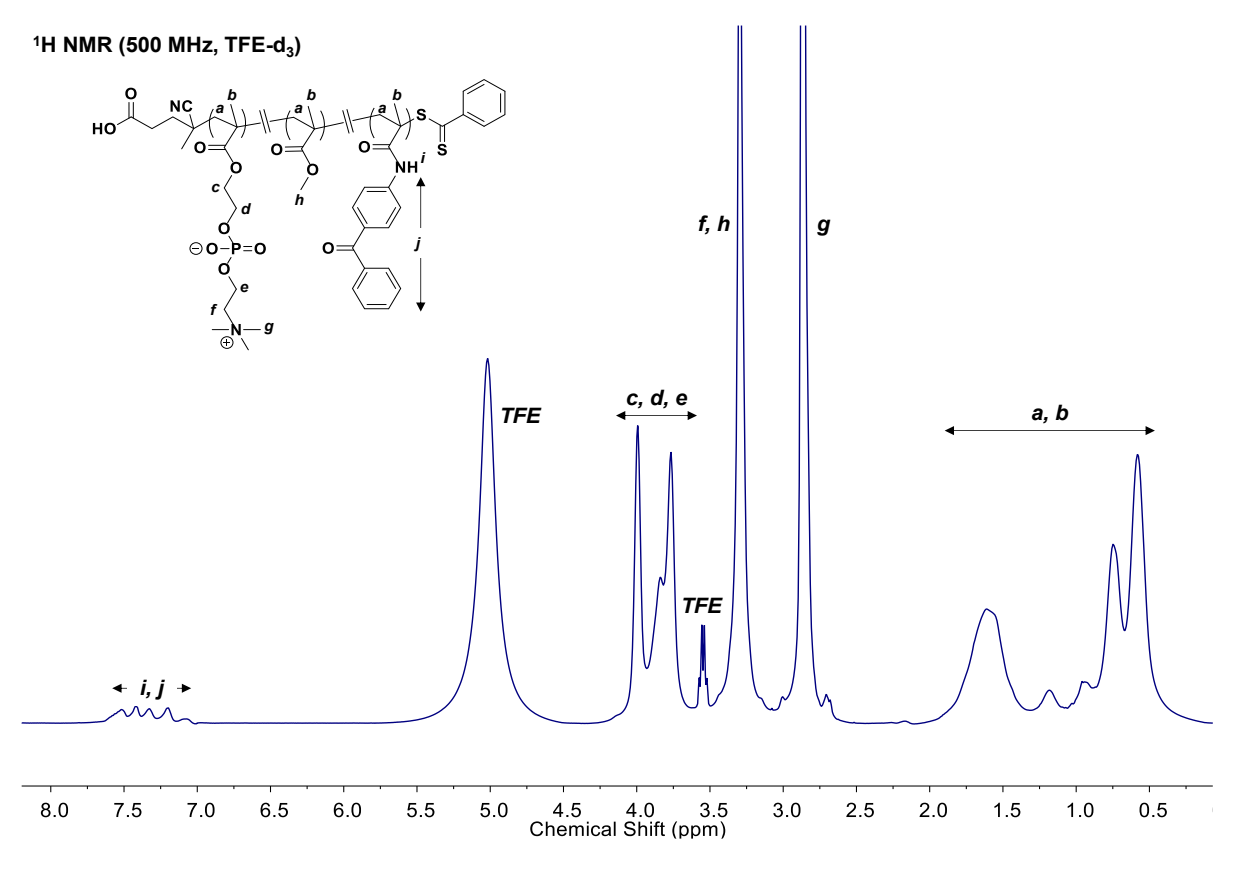


Figure S1. ¹H NMR spectrum of P(MPC-MMA-BPMA) (TFE-d₃, 500 MHz).

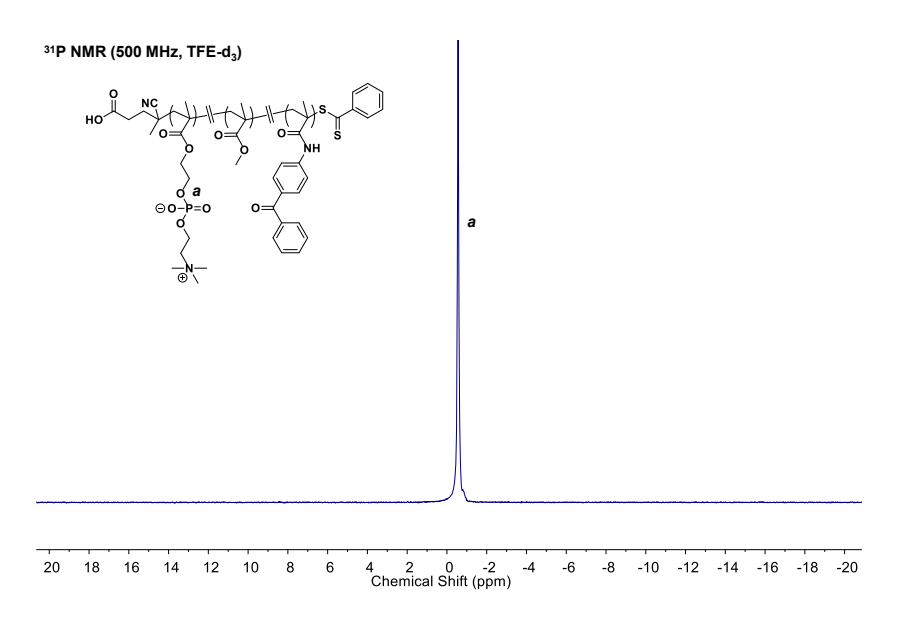


Figure S2. ³¹P NMR spectrum of P(MPC-MMA-BPMA) (TFE-d3, 500 MHz).

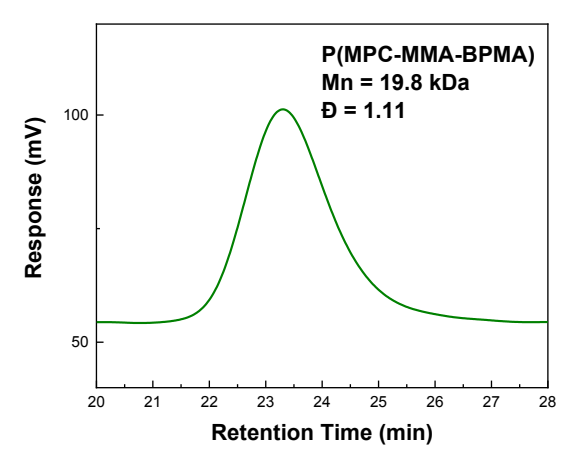


Figure S3. SEC trace of P(MPC-MMA-BPMA) eluting in TFE. M_n and $\mathfrak D$ were estimated using PMMA standards.

2. Preparation of E-beam patterned PMPC @ Graphene

Graphene was synthesized by chemical vapor deposition (CVD) method with some adaptations as described by others.² Following transfer onto a Si/SiO₂ substrate (300 nm oxide, Siltronix), a solution of 10 mg/mL of PMPC in 2,2,2-trifluoroethanol (TFE) was spin-cast (500 rpm/5 s, 4000 rpm/45 s). The sample was then patterned by e-beam lithography (EBL), with a dosage of 350 $\frac{\mu c}{cm^2}$ and subsequently developed with methyl isobutyl ketone/isopropanol solution (MIBK/IPA 1:3, Micro Chem) for 2 minutes to remove unexposed regions. The sample was then soaked in IPA (CMOS grade, J.T.Baker) for 30 sec and dried with nitrogen flow.

3a. Preparation of normal orientation sample

Following the steps outlined in 2, gold contacts were deposited by electron-beam evaporation through a mask. The sample and substrate were adhered to a Ni/Fe AFM sample disk with a 2-sided copper tape, and the contacts were wire-bonded to the sample disk with 6-8 microscopic wire leads.

3b. Inversion of patterned graphene and contact formation

Following the steps outlined 2, a layer of polycarbonate was cast over the sample and baked in 150°C on a hot plate for 2 minutes. Next, the oxide layer of the underlying Si/SiO₂ substrate was etched away by buffered oxide etch (BOE 6:1, J.T.Bakers), leaving a free-standing graphene/PMPC/polycarbonate membrane floating at the solution's surface while the oxide-free silicon substrate had sunk to the bottom. The floating membrane of graphene/PMPC was then collected and thoroughly washed with DI water and blow-dried with N₂. The free-floating membrane was then inverted onto a fresh Si/SiO₂ substrate.

Electrical gold contacts were evaporated onto the sides of the graphene sample through a mask and sample mounting was then carried out in an analogous fashion to 3a.

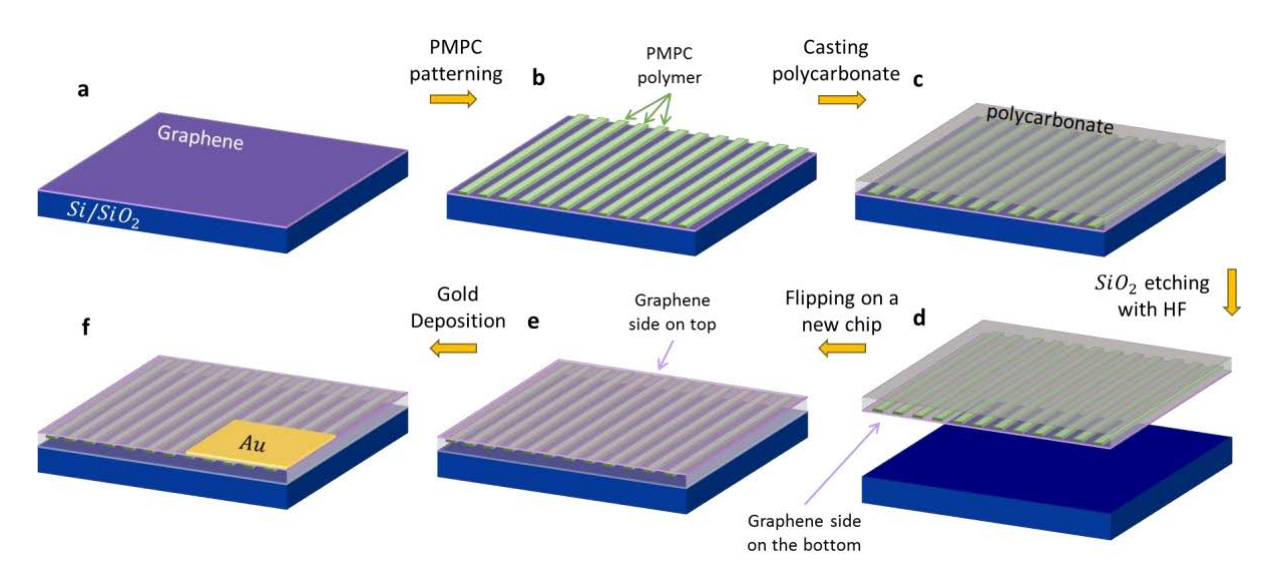


Figure S4. Schematic illustration of the flipping process for accurate measurement of the material work function by KPFM. a) Graphene was transferred on a Si/SiO₂ chip. b) PMPC polymer was patterned on top of the graphene. c) Polycarbonate layer was spin-casted on the graphene. d) The oxide layer of the Si/SiO₂ chip was etched by HF. e) The polycarbonate-PMPC-Graphene membrane was flipped on a new chip so that the graphene side was on top. f) A gold electrode was deposited on top on the graphene for grounding purposes.

3c. Preparation of PMPC-covered Devices for transport measurements

CVD-grown graphene was transferred to a Si/SiO₂ substrate with 300 nm of oxide layer, as in **2**. Graphene was shaped by spin-casting AZ nlof negative resist (Merck), patterned with EBL, developed with AZ 726 developer (Merck), and then treated with oxygen plasma (20 sccm) for 30s to remove unwanted graphene. The AZ resist was then removed by soaking in dimethyl sulfoxide (DMSO, Merck)

at 80°C for 1h. Contacts were formed by first spin-casting PMMA, patterning with EBL and developing with MIBK. Contacts were then deposited by electron-beam deposition of 3 nm Cr and 70 nm Au, and finally liftoff was performed in acetone with stirring at 250 rpm. The PMPC solution was spin-cast, patterned and developed on the chip as described in section 2. The chip was then mounted on a chip carrier and wire-bonded to it.

4. KPFM of Normal and Inverted patterned PMPC/graphene with contacts

Samples were analyzed using a Dimension Bioscope AFM with a Nanoscope IIIa controller, using 2-pass lift mode AM-KPFM, and with vibration isolation via a Minus K BM-8 platform placed within a Herzan The Crypt acoustic enclosure. AppNano ANSCM-PT probes were used for all measurements, which consist of an ~225 mm long Si cantilever that has been coated with PtIr, resulting in tips with ~30nm radius and a resonant frequency of ~75 kHz. Measurements were performed with scan sizes of between 10 and 100 mm, at speeds between 0.4 and 1.5 Hz, and with a lift height of 30 nm. Analysis of topography images was performed in Gwyddion, by performing row alignment and plane subtraction, and analysis of SPC images by row alignment only or no processing.

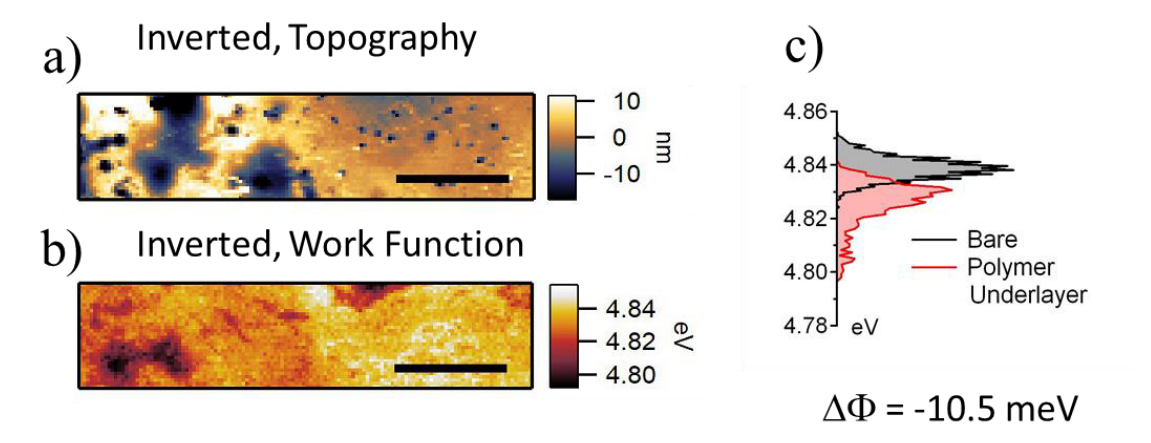


Figure S5. (a) Topography and (b) work function maps of the inverted PMPC@graphene sample, scale bars indicate 5 μ m. (c) Work function distributions graphene with and without a zwitterionic polymer underlayer. Here graphene is facing the KPFM probe, and PMPC is underneath.

To demonstrate the observed surface potentials in previous measurements were due to an electronic interaction between PMPC and graphene, KPFM was performed on PMPC drop cast onto a cleaned ITO slide. The curved edge of the dried droplet was located, which shows small PMPC features. The bare portion of the ITO was used for in situ work function calibration ($\Phi = 4.78 \text{ eV}$). The effect of PMPC was determined to be very small, -12 meV.

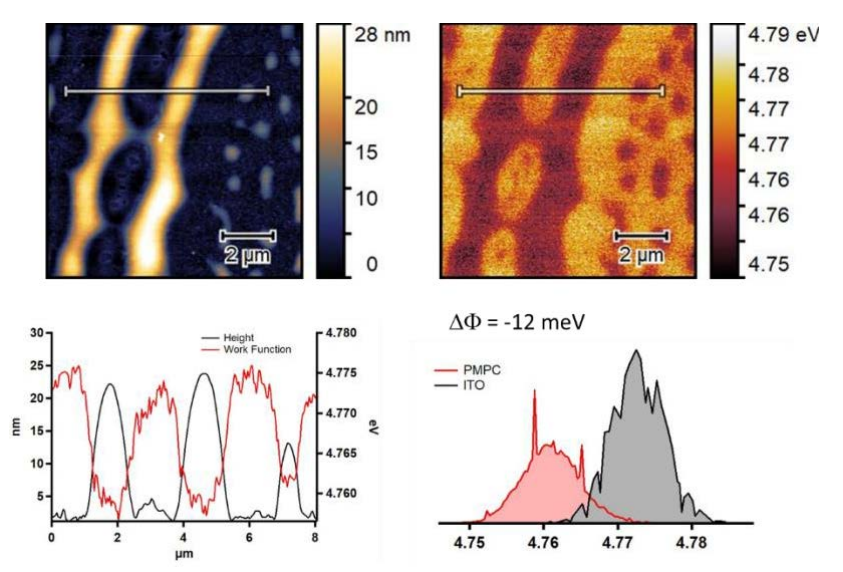


Figure S6. Control KPFM measurement of PMPC drop cast on ITO. Topography and calibrated work function maps (upper left and right, respectively). Line profiles (below left), and work function distributions (below right).

5. EFM of patterned PMPC/graphene with contacts

The same Dimension Bioscope and ANSCM-PT probes were used for EFM measurements. 2-pass EFM was performed using a 30 nm lift height, with a bias varied between -8V and +8V applied to the probe and with a grounded sample. The collection of phase shift images recorded for each sample were processed in Mathematica, fitting a quadratic function of voltage at each spatial location in the images. The conventional model³ of tip response to electric field gradients in the z direction is expressed as:

$$\Delta \varphi = -\frac{Q}{k} \frac{dF}{dz} = -\frac{Q}{k} \left(\frac{3\alpha}{z^4} V_{tip}^2 - q \frac{\left(V_{tip} - V_0 \right)}{z^2} \right)$$

The linear term incorporating the voltage encodes information on density of free charges, and the quadratic term relates phase-shift to the polarizability of the sample (at the tip resonance frequency). A representative fit from a point in the PMPC-coated region of the normal orientation is shown in Figure S7.

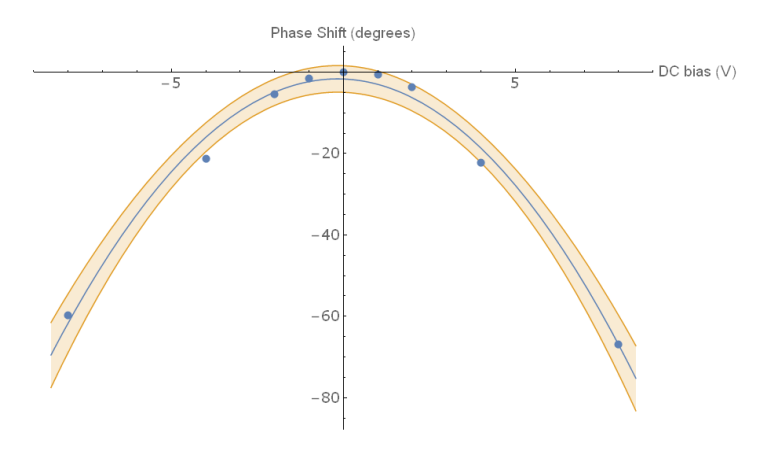


Figure S7. EFM Phase shift vs. DC bias taken from the normal orientations sample, with a quadratic fit and bands indicating 95% confidence interval.

6. Statistical Comparison of EFM Results

Calculation of the two-portion z-statistic⁴ indicates that the change in polarizability was highly significant in both samples at the 99% confidence level, from values of 5.41 and 6.67 for normal and inverted samples, respectively. However only in the normal orientation sample was there a significant change in surface charge as judged by the same two-portion z-statistic, 29.8 for the normal sample but only 0.73 for the inverted sample.

7. Computational Methods for PMPC/graphene

The Vienna Ab Initio Simulation Package (VASP) was used to perform non-spin-polarized planewave DFT calculations.^{5,6} The projector-augmented wave (PAW) method^{7,8} was used to describe the core and valence electrons, and the generalized-gradient approximation in the Perdew-Burke-Ernzerhof (PBE) form⁹ was used to describe electron exchange and correlation. Dispersion interactions were taken into account by applying Grimme's PBE-D3 corrections.¹⁰ The kinetic energy cutoff was set to 400 eV and the Gaussian smearing of 0.05 eV was used for Brillouin-zone integrations. Atomic positions were optimized using the conjugate-gradient method with a force tolerance of 0.02 eV/Å. The graphene sheet was modelled as a 6×6 supercell with a single adsorbed zwitterionic moiety leading to a nominal surface coverage of 5.299×10^{13} cm⁻². To avoid spurious interactions between periodic images, at least 15 Å of vacuum was inserted normal to the graphene sheet. Dipole corrections were applied in all calculations along the direction normal to the graphene sheet. Dipole corrections were sampled with a Γ -centered κ -point mesh; a $3\times3\times1$ mesh was used for relaxation calculations followed by electronic structure calculations using a dense $13\times13\times1$ mesh. The density of states were calculated using the tetrahedron smearing method with Blöchl corrections¹³ and the smearing width of 0.1 eV.

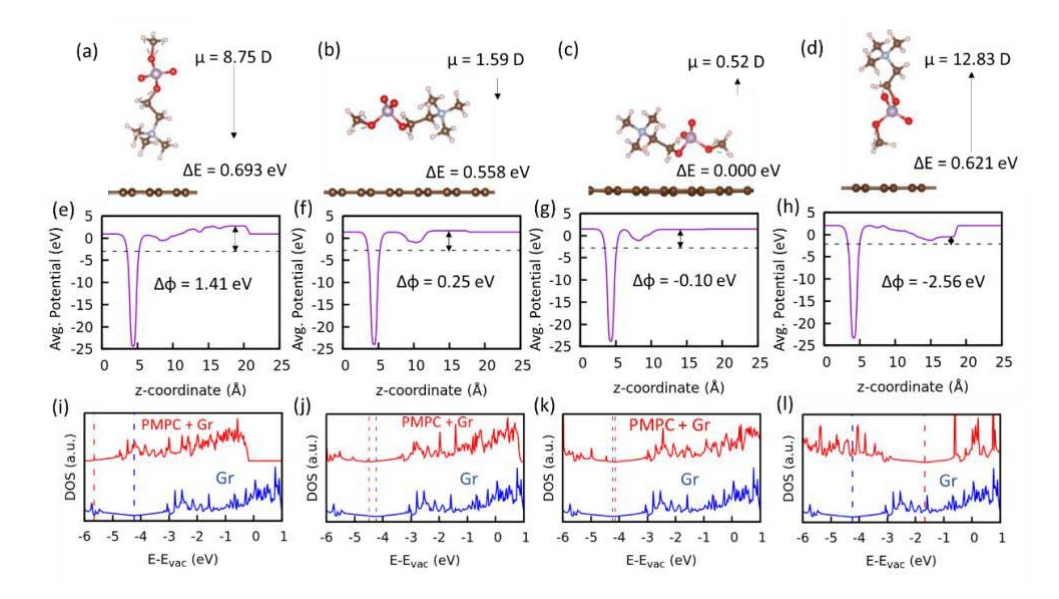


Figure S8. (a)-(d) Various orientations of the dipolar pendant moiety on graphene: arrows indicate the direction of the dipole moment (μ) with magnitudes (in Debyes) as indicated; ΔE is the relative energy of each of these structures with respect to lowest energy structure in (c). (e)-(h) Planar-averaged Hartree potential for each of the configurations shown in the panel immediately above; work function shifts (with respect to bare graphene ($\Phi = 4.24 \text{ eV}$) for each orientation are indicated. (i)-(l) Total density of states (DOS) plots corresponding to the respective configurations immediately above in panels (a-d); DOS in red and blue correspond to graphene with and without the adsorbed moiety, respectively, while dotted lines indicate the Fermi levels for in each case; all energies are reported with respect to the vacuum level ($E_{\text{vac}} = 0 \text{ eV}$).

8. PMPC/graphene devices transport results

Transport measurements were performed under vacuum using a Montana Instruments cryostation at room temperature on three devices with different PMPC coverage. The I-V measurements were measured by the four-point probe method with a Keysight B2912 source measure unit. Using this method, the sheet conductance, σ , for each device can be extracted. The mobility, μ , could then be calculated by:¹⁴

$$\mu = \frac{\sigma}{nq}$$

where q the elementary electric is charge, and n is the carrier charge density given by:

$$n = \frac{C_g (V_g - V_{Dirac})}{q}$$

Here C_g is the gate capacitance, V_g is the gate voltage, and V_{Dirac} is the voltage at which the conductance is at its minimum, indicating the Dirac point.

References

- (1) Kim, J.; Hanna, J. A.; Byun, M.; Santangelo, C. D.; Hayward, R. C. Designing Responsive Buckled Surfaces by Halftone Gel Lithography. *Science* (80-.). **2012**, 335 (6073), 1201 LP 1205.
- (2) Yu, Q.; Jauregui, L. A.; Wu, W.; Colby, R.; Tian, J.; Su, Z.; Cao, H.; Liu, Z.; Pandey, D.; Wei, D.; et al. Control and Characterization of Individual Grains and Grain Boundaries in Graphene Grown by Chemical Vapour Deposition. *Nat. Mater.* **2011**, *10* (6), 443–449.
- (3) Kim, J.; Jasper, W. J.; Hinestroza, J. P. Charge Characterization of an Electrically Charged Fiber via Electrostatic Force Microscopy. *J. Eng. Fiber. Fabr.* **2006**, *I* (2), 155892500600100200.
- (4) Montgomery, D. C.; Runger, G. C. *Applied Statistics and Probability for Engineers*, 6th ed.; John Wiley & Sons, 2014.
- (5) Kresse, G.; Furthmüller, J. Efficiency of Ab-Initio Total Energy Calculations for Metals and Semiconductors Using a Plane-Wave Basis Set. *Comput. Mater. Sci.* **1996**, *6* (1), 15–50.
- (6) Kresse, G.; Furthmüller, J. Efficient Iterative Schemes for Ab Initio Total-Energy Calculations Using a Plane-Wave Basis Set. *Phys. Rev. B* **1996**, *54* (16), 11169–11186.
- (7) Blöchl, P. E. Projector Augmented-Wave Method. *Phys. Rev. B* **1994**, *50* (24), 17953–17979.
- (8) Kresse, G.; Joubert, D. From Ultrasoft Pseudopotentials to the Projector Augmented-Wave Method. *Phys. Rev. B* **1999**, *59* (3), 1758–1775..
- (9) Perdew, J. P.; Burke, K.; Ernzerhof, M. Generalized Gradient Approximation Made Simple. *Phys. Rev. Lett.* **1996**, 77 (18), 3865–3868..
- (10) Grimme, S.; Antony, J.; Ehrlich, S.; Krieg, H. A Consistent and Accurate Ab Initio Parametrization of Density Functional Dispersion Correction (DFT-D) for the 94 Elements H-Pu. *J. Chem. Phys.* **2010**, *132* (15), 154104...

- (11) Makov, G.; Payne, M. C. Periodic Boundary Conditions in *Ab Initio* Calculations. *Phys. Rev. B* **1995**, *51* (7), 4014–4022.
- (12) Neugebauer, J.; Scheffler, M. Adsorbate-Substrate and Adsorbate-Adsorbate Interactions of Na and K Adlayers on Al(111). *Phys. Rev. B* **1992**, *46* (24), 16067–16080..
- (13) Blöchl, P. E.; Jepsen, O.; Andersen, O. K. Improved Tetrahedron Method for Brillouin-Zone Integrations. *Phys. Rev. B* **1994**, *49* (23), 16223–16233.
- (14) Tan, Y.-W.; Zhang, Y.; Bolotin, K.; Zhao, Y.; Adam, S.; Hwang, E. H.; Das Sarma, S.; Stormer, H. L.; Kim, P. Measurement of Scattering Rate and Minimum Conductivity in Graphene. *Phys. Rev. Lett.* **2007**, *99* (24), 246803.